Geological Society, London, Special Publications Online First

Age relationships of the Rembrandt basin and Enterprise Rupes, Mercury

Sabrina Ferrari, Matteo Massironi, Simone Marchi, Paul K. Byrne, Christian Klimczak, Elena Martellato and Gabriele Cremonese

Geological Society, London, Special Publications, first published July 29, 2014; doi 10.1144/SP401.20

Notes

Age relationships of the Rembrandt basin and Enterprise Rupes, Mercury

SABRINA FERRARI[1]*, MATTEO MASSIRONI[1,2], SIMONE MARCHI[3], PAUL K. BYRNE[4,5], CHRISTIAN KLIMCZAK[4], ELENA MARTELLATO[2,6] & GABRIELE CREMONESE[2]

[1]*Department of Geosciences, University of Padua, via Gradenigo 6, 35131 Padova, Italy*

[2]*Astronomical Observatory of Padua, INAF, Vic. Osservatorio 5, 35122 Padova, Italy*

[3]*NASA Lunar Science Institute, Southwest Research Institute, 1050 Walnut Street, Boulder, CO 80302, USA*

[4]*Department of Terrestrial Magnetism, Carnegie Institution of Washington, 5241 Broad Branch Road NW, Washington, DC 20015-1305, USA*

[5]*Lunar and Planetary Institute, Universities Space Research Association, 3600 Bay Area Boulevard, Houston, TX 77058, USA*

[6]*Department of Physics and Astronomy, University of Padua, via Marzolo 8, 35131 Padova, Italy*

**Corresponding author (e-mail: sabrina.ferrari@studenti.unipd.it)*

Abstract: The Rembrandt basin is the largest well-preserved impact feature in the southern hemisphere of Mercury. Its smooth volcanic infill hosts wrinkle ridges and graben, and the entire basin is cross-cut by the Enterprise Rupes scarp system. On the basis of the Model Production Function crater chronology, our analysis shows that the formation of the Rembrandt basin occurred at 3.8 $\pm$ 0.1 Ga during the Late Heavy Bombardment, consistent with previous studies. We also find that the smooth plains interior to the basin were emplaced between 3.7 and 3.6 $\pm$ 0.1 Ga, indicative of a resurfacing event within the Rembrandt basin that is consistent with the presence of partially buried craters. These youngest plains appear temporally unrelated to basin formation, and so we regard their origin as likely to be due to volcanism. We identify the same chronological relationship for the terrain cross-cut by Enterprise Rupes to the west of the basin. Therefore, volcanic activity affected both the basin and its surroundings, but ended prior to the majority of basin- and regional-scale tectonic deformation. If Enterprise Rupes formed prior to the Rembrandt basin, then regional-scale tectonic activity along this structure might have lasted at least 200 myr.

Our current understanding of the early surface of Mercury involves a primitive crust that experienced intense cratering during the Late Heavy Bombardment (LHB) approximately 4.1–3.6 Ga ago (e.g. Tera *et al.* 1974; Strom & Neukum 1988; Marchi *et al.* 2013*a*). Concurrent crustal shortening due to the global cooling-induced contraction of the planet led to the formation of thrust fault-related landforms (lobate scarps and wrinkle ridges: e.g. Watters *et al.* 2004). Extensive smooth deposits, the majority of which are interpreted to be volcanic (Head *et al.* 2009 and references therein; Prockter *et al.* 2010), that covered some 27% of the planet's surface (Denevi *et al.* 2013) were also emplaced. Activity on some lobate scarps continued beyond the emplacement of the youngest volcanic smooth plains (Strom *et al.* 1975; Melosh & McKinnon 1988; Watters *et al.* 2009*c*; Head *et al.* 2009).

Notably, some tectonic deformation on Mercury is manifest in spatially coherent patterns. The distinctive arrangement of structures observed within volcanically infilled and buried impact basins and craters on Mercury (Watters *et al.* 2009*b*, 2012; Head *et al.* 2011; Fassett *et al.* 2012; Klimczak *et al.* 2012) may have resulted from the cooling of low-viscosity lava flows emplaced as rapidly accumulated, thick units against a backdrop of pervasive global contraction (Freed *et al.* 2012; Watters *et al.* 2012). Within the largest basins in particular, the load of volcanic infill could have induced subsidence and, consequently, the formation of radial and concentric wrinkle ridges (Watters *et al.*

From: Platz, T., Massironi, M., Byrne, P. K. & Hiesinger, H. (eds) *Volcanism and Tectonism Across the Inner Solar System*. Geological Society, London, Special Publications, **401**, http://dx.doi.org/10.1144/SP401.20

2009*b*, 2012), whereas vertical motion (Dzurisin 1978; Melosh & Dzurisin 1978; Blair *et al.* 2013) or inward flow of lower crustal material triggered by basin formation (Watters *et al.* 2005; Watters & Nimmo 2010) could have promoted subsequent uplift of basin centres and the formation of radial and concentric graben (Watters *et al.* 2009*c*; Klimczak *et al.* 2010; Byrne *et al.* 2013). Alternatively, such distinctive patterns of extensional features in Mercury's largest impact basins may have formed due to the thermal contraction of rapidly emplaced lava flow on the basin floor (Freed *et al.* 2012; Byrne *et al.* 2013). Nevertheless, patterns of deformation that include basin-radial and -concentric faulting were probably controlled by the shape of the impact structure itself.

Such a systematic pattern is preserved in the 715 km-diameter Rembrandt basin. Imaged for the first time during the second flyby of the MErcury Surface, Space ENvironment, Geochemistry, and Ranging (MESSENGER) spacecraft, most of the basin interior is covered by smooth, high-reflectance plains interpreted to be of volcanic origin (Denevi *et al.* 2009; Watters *et al.* 2009*a*). Similar high-reflectance plains are broadly distributed across the surface of Mercury, and have also been recognized in the surroundings of the Rembrandt basin (Denevi *et al.* 2013).

The smooth-plains infill of the Rembrandt basin hosts sets of basin-radial and -concentric contractional and extensional tectonic structures (Fig. 1a, b). This pattern resembles to first order the arrangement of structures within the Caloris basin, the largest preserved impact structure on Mercury (Murchie *et al.* 2008; Watters *et al.* 2009*b*; Byrne *et al.* 2012), in which individual sets of radial and concentric landforms are most probably due to multiple episodes of deformation (Strom *et al.* 1975; Melosh & McKinnon 1988; Watters *et al.* 2005, 2009*c*; Klimczak *et al.* 2010). Notably, the Rembrandt basin and its smooth plains are cross-cut by an 820 km-long scarp system (Watters *et al.* 2009*a*; Byrne *et al.* 2014), which trends approximately east–west outside the basin before bending towards the NE within the basin itself (white arrows in Fig. 1a). The individual faults of this system, collectively named Enterprise Rupes, accommodated crustal shortening that likely resulted from the global contraction of Mercury as its interior cooled (Watters *et al.* 2009*c*), perhaps augmented by other processes such as mantle convection and tidal de-spinning (Massironi *et al.* 2014). It is probable that the current shape of the reverse fault system, and particularly its northwards bend, was influenced by the formation of the Rembrandt basin. Ferrari *et al.* (2012) suggested that the branch of Enterprise Rupes outside the Rembrandt basin predates the basin-forming impact, as part of a pre-existing scarp system. The basin-forming impact partially overprinted that system, and induced a perturbation of the prevailing stress field that reorientated the strike of the new branch as it grew within the new basin. This scenario accounts for the different orientations of the portions of Enterprise Rupes outside and inside the basin, and predicts differences in vertical displacements between those segments that have been observed (Ferrari *et al.* 2012).

The Rembrandt basin and its surrounding region were probably affected by many of the processes that modified the surface of Mercury (i.e. subsequent impacts in general, global- and basin-scale tectonic deformation, and volcanic resurfacing), and so it is a suitable case-study location for understanding the sequence and duration of such processes. In this study, we aim to establish a chronological sequence of formation for the surface units and structures of the Rembrandt basin and its surroundings. We therefore performed crater counts on different type units in the area in order to estimate the absolute model ages by applying the Model Production Function (MPF) of Marchi *et al.* (2009, 2012, 2013*b*), complemented by identified cross-cutting and superposition relationships, to determine the relative timing of terrain and structure formation within and surrounding the Rembrandt basin.

Geological units and cross-cutting relationships in and around the Rembrandt basin

The geological sketch of the region that includes the Rembrandt basin and Enterprise Rupes in Figure 1b was compiled from data returned by the MESSENGER spacecraft during its flyby and orbital phases. The map consists of internal basin units, the basin's proximal ejecta, superposed impact craters and their ejecta deposits, and prominent tectonic structures. The MESSENGER Mercury Dual Imaging System (MDIS) solar-day-one monochrome base map mosaic (with an average spatial resolution of 250 m/pixel) (Hawkins *et al.* 2007), together with the wide-angle camera (WAC) multispectral mosaic base map (bands 1000, 750, and 430 nm; average spatial resolution 1000 m/pixel) were analysed in the ESRI® ArcMap geographical information system (GIS) environment. The MDIS orbital datasets were complemented with flyby narrow-angle camera (NAC) images taken under illumination conditions that better show landforms with subtle topographical expressions. Single images were processed with the open-access USGS Integrated Software for Imagers and Spectrometers (ISIS) software. Mapped units were classified on the basis of their surface textures and stratigraphic

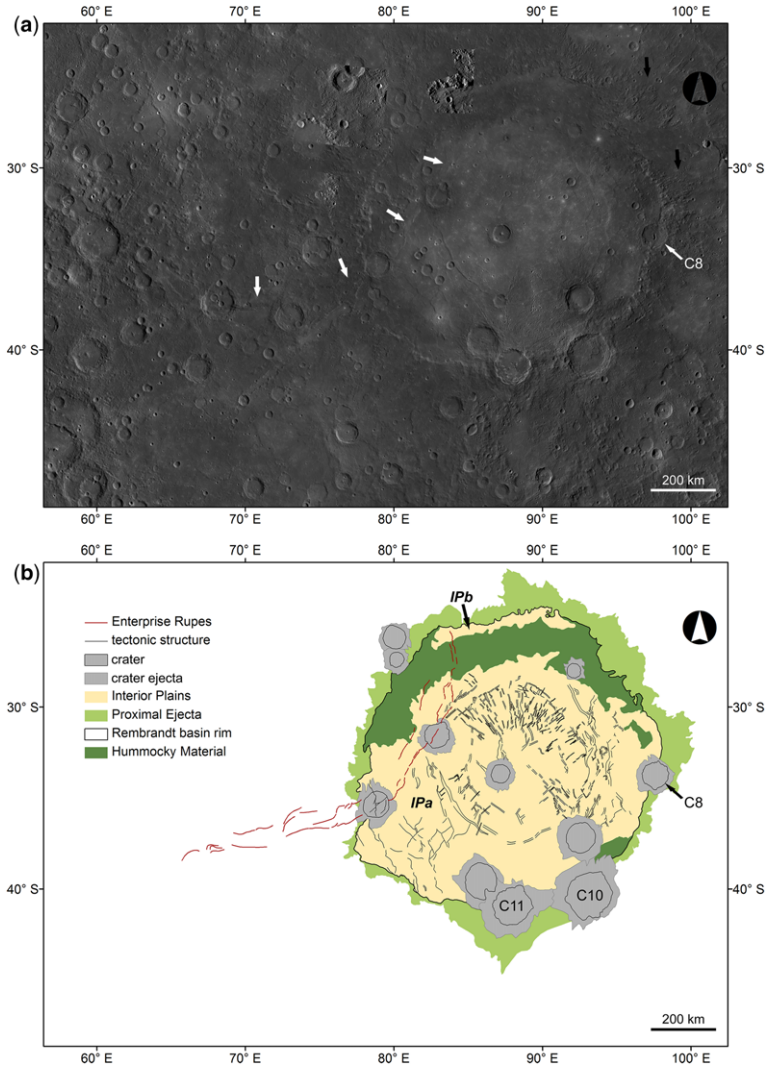

Fig. 1. The Rembrandt basin and Enterprise Rupes. (**a**) MESSENGER MDIS monochrome base map, shown with a Mercator projection centred on Rembrandt (33°S, 88°E); white arrows point to Enterprise Rupes and black arrows indicate radially lineated basin ejecta. (**b**) Geological sketch map showing the variety of units of the Rembrandt basin and its superposed structures.

relationships: the 'Hummocky Material' and the 'Interior Plains' units fill the basin, whereas the 'Proximal Ejecta' unit surrounds the basin rim (Fig. 1b).

The Hummocky Material unit (81 000 km^2 in area) probably consists of a mixture of impact melt and ejecta deposits (breccias) that formed hills, depressions and high-standing knobs, morphological features characteristic of ejecta deposited during the formation of large basins of the Moon (e.g. Cintala & Grieve 1998) and the Caloris basin on Mercury (Fassett *et al.* 2009; Denevi *et al.* 2013). This texture was initially recognized within the Rembrandt basin by Watters *et al.* (2009*a*). The Hummocky Material unit is mostly buried by the smooth Interior Plains deposits or, along the southern rim, appears strongly reworked by subsequent impact events (e.g. craters C10 and C11 in Fig. 1b) that make a clear demarcation of the unit difficult.

Beyond the basin rim, radially lineated terrain (black arrows in Fig. 1a) has been interpreted as basin ejecta (Watters *et al.* 2009*a*), of which the Proximal Ejecta unit (132 000 km^2 in area)

represents the coherent material that surrounds almost the entire rim crest. It was probably emplaced contemporaneously with the Hummocky Material unit.

The smooth Interior Plains deposits (370 000 km^2 in cumulative area) have a higher reflectance than the basin formation-related units, and are likely to be volcanic in origin (Denevi *et al.* 2009; Watters *et al.* 2009*a*). This unit covers most of the basin floor but occurs as two discontinuous exposures (which we label as '*IPa*' and '*IPb*' in Fig. 1b). IPa is the most extensive exposure (357 000 km^2) and covers the central portion of the basin, extending from the western to the eastern rims; IPb occurs as a much smaller patch (12 000 km^2) that embayed the northern basin rim wall.

MESSENGER colour data (Fig. 2) indicate that the IPa sub-unit shows subtle variations in tone. Colour variations on Mercury can be attributed to different surface compositions (Robinson & Lucey 1997; Blewett *et al.* 2007; Robinson *et al.* 2008; Murchie *et al.* 2008). On the SW basin rim, the IPa sub-unit darkens and becomes texturally indistinguishable from the surface immediately exterior to the basin (the dark cross symbols in Fig. 2 indicate the point where the IPa sub-unit gradually darkens towards the basin perimeter), suggesting that the interior smooth plains and the surrounding terrain may be compositionally similar. This portion of terrain exterior to the basin also displays several patches of higher reflectance smooth plains, mainly associated with large craters and within a prominent trough radial to Rembrandt (white arrows in Fig. 2). The reflectance of those patches is similar to those within the Interior Plains, and both host several partly buried craters (craters marked with black arrows in Fig. 2), which attest to substantial volcanic (Denevi *et al.* 2009, 2013) resurfacing after their formation. A pit-floor crater situated in the 60 km-diameter crater C8 of Figure 1a (Denevi *et al.* 2013) may represent a source vent from which effusive volcanism erupted, at least for the

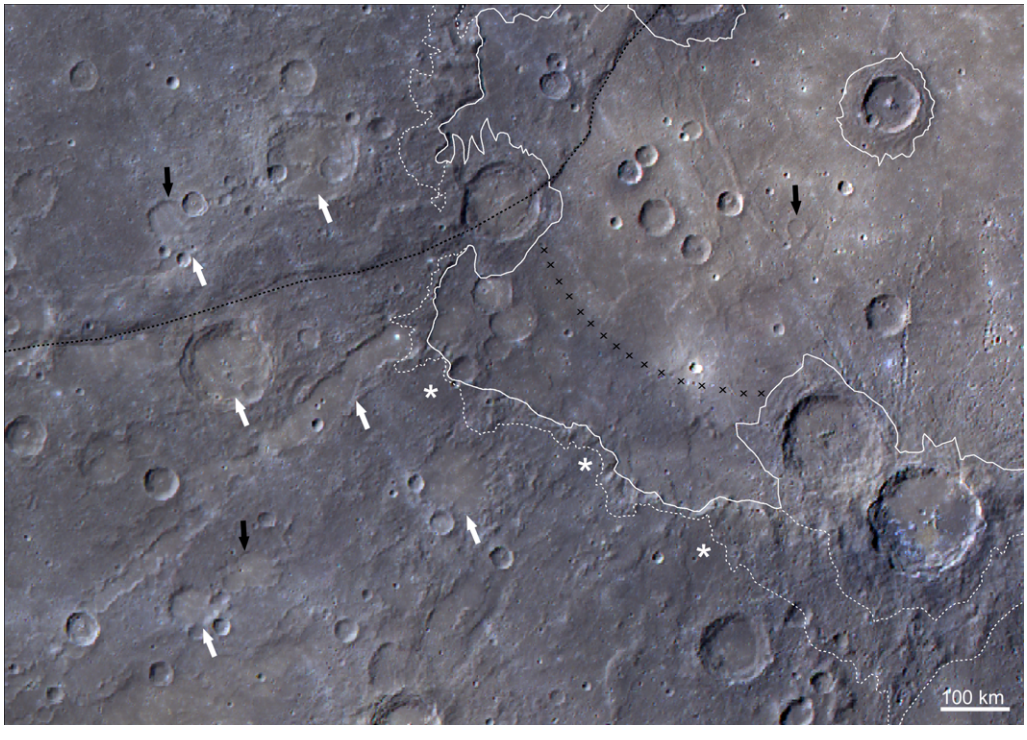

Fig. 2. MESSENGER MDIS WAC multispectral mosaic (bands 1000, 750 and 430 nm; average spatial resolution is 1000 m/pixel) of the SW boundary of Rembrandt basin. The arcuate line of black crosses indicates the transition of surface reflectance within the expansive Interior Plains sub-unit (IPa, white boundary): while retaining the same texture, the surface becomes darker towards the basin perimeter. High-reflectance plains, such as the Interior Plains and several smaller, outlying patches (white arrows), partially filled craters (black arrows) and reduced ejecta proximal to the basin (white dashed boundary), suggest resurfacing for both the Interior Plains deposits and the units to the west/SW. Enterprise Rupes (black dashed line) deformed most of the units shown here.

basin interior. It is entirely possible, however, that the vents from which these lavas issued may be located both within and outside the basin, but have been obscured by subsequent flows.

Moreover, at the footwall of Enterprise Rupes (black dotted line, Fig. 2), the Proximal Ejecta unit appears either to be texturally smooth or entirely absent (white stars, Fig. 2), which suggests that volcanic resurfacing of the Exterior Plains unit also occurred. However, both the basin-radial and -concentric contractional and extensional tectonic structures, and Enterprise Rupes itself, deform the Rembrandt basin's Interior Plains unit, and so at least the most recent activity of each of these tectonic systems must post-date the emplacement of the Interior Plains unit (Fig. 1b).

The Model Production Function chronology applied to the surface of Mercury

The age estimation of geological units on airless planetary bodies using crater size–frequency distributions (SFDs) is based on the tenet that older surfaces have accumulated more craters than younger surfaces. Ages for the Rembrandt basin units have been calculated by means of the Model Production Function (MPF) chronology for Mercury (Marchi *et al.* 2009; Massironi *et al.* 2009), which relies on models of the impactor flux on the planet. This flux is converted into the expected crater SFD per unit time and per unit surface by the crater-scaling law of Holsapple & Housen (2007), which takes into account the properties of the materials involved. Then the cumulative number of 1 km-diameter craters is calibrated using radiometric ages and crater densities observed at the Apollo and Luna landing sites on the Moon, in order to determine the absolute age calibration.

Two key features of the MPF method are: (i) the distinction between Main Belt Asteroids (MBA) and Near Earth Objects (NEO) as impactor size–frequency distributions; and (ii) the use of a crater-scaling law, which allows for the computation of the transient crater diameter, D_t, as a function of impactor size, d, and impact parameters, as well as of target properties. The equation for the crater-scaling law adopted from Holsapple & Housen (2007) is:

$$D_t = kd\left[\frac{gd}{2v_{\downarrow}^2}\left(\frac{\rho}{\delta}\right)^{\frac{2\nu}{\mu}} + \left(\frac{Y}{\rho v_{\downarrow}^2}\right)^{\frac{2+\mu}{2}}\left(\frac{\rho}{\delta}\right)^{\frac{\nu(2+\mu)}{\mu}}\right]^{-\left(\frac{\mu}{2+\mu}\right)} \quad (1)$$

where g is the target gravitational acceleration of the planet, $v_{\downarrow}$ is the perpendicular component of the impactor velocity, δ is the projectile density, ρ and Y are the density and tensile strength of the target, respectively, k and μ depend on the cohesion of the target material, and ν depends on the porosity of the target material (Table 1). As discussed by Marchi *et al.* (2009, 2011), the density, strength and cohesion of Mercury's crust are expected to vary as a function of depth, as has been inferred for these properties on the Moon (Toksöz *et al.* 1973; Hörz *et al.* 1991). Hence, different ranges of strength and density of the target material must be considered according to the size of the impactor, and a transition of the crater-scaling law from shallower 'cohesive soil' (i.e. reworked by impact gardening) to deeper 'hard rock' can be used. Impact and target parameters used in this study for both regimes are listed in Table 1.

The transient crater diameter, D_t, is converted to a *final* crater diameter, D, according to the following expressions:

$$D = 1.3D_t \quad \text{if } D_t \leq D_*/1.3 \quad (2)$$

and

$$D = 1.4{D_t}^{1.18}/{D_*}^{0.18} \quad \text{if } D_t > D_*/1.3. \quad (3)$$

Here, D_* is the observed simple-to-complex transition crater diameter, which for Mercury corresponds to 11 km (Pike 1988). The factors adopted for these estimates are described in detail in Marchi *et al.* (2011).

Based on these calculations, age assessments are performed assuming a specific rheological layering

Table 1. *Parameters used for the crater-scaling law of Holsapple & Housen (2007)*

	Impactor density (g cm^{-3}) δ	Constant k	Scaling exponent μ	Scaling exponent ν	Target density (g cm^{-3}) ρ	Target tensile strength (MPa) Y
Cohesive soil (gravity regime)	2.6	1.03	0.41	0.4	2.8	2
Hard rock (strength regime)		0.93	0.55			20

for each mapped unit. For instance, the mixture of impact melt and ejecta formed during a giant impact should be less cohesive than the basement on which it lies (i.e. ejecta over a deeply fractured horizon). Conversely, a basin's volcanic infill probably partly or even entirely strengthens the pre-existing fractured layer at the basin floor, such that a cohesionless stratum might be confined to a thin regolith cover. The depth of transition from one regime to another can be considered to be reflected by an S-shaped kink in crater SFDs, to which an appropriate MPF curve can be fitted (Massironi *et al.* 2009). The depth of transition (H) can be inferred by the crater size corresponding to the centre of the S-shaped kink. Following Marchi *et al.* (2011), we assume that the kink occurs at $D_t \sim 4H$.

However, S-shaped kinks can also arise from a loss of craters due to different resurfacing processes (Platz *et al.* 2013). Neukum & Horn (1975) assumed that observable kinks in crater SFDs determined for lunar surfaces are always markers of resurfacing, even in those cases where the morphological signature of later lava flows (and thus resurfacing) is not observed. In such cases, kinks are regarded as indications of composite SFDs in which smaller craters reflect the age of younger units and larger craters indicate the age of older units. Neukum & Horn (1975), however, considered that crater SFD S-shaped kinks depend solely on volcanic resurfacing, whereas MPFs attribute the kinks to either rheological layering (i.e. fractured material over hard rock) or to resurfacing. Thus, in order to derive a more accurate age estimate using MPF, it is a fundamental requirement that the crater production function be placed in the geological context of the units being investigated.

MPF applied on the Rembrandt area

We performed crater counts on the geological units described above, in the areas shown in Figure 3, using a portion of the global monochrome

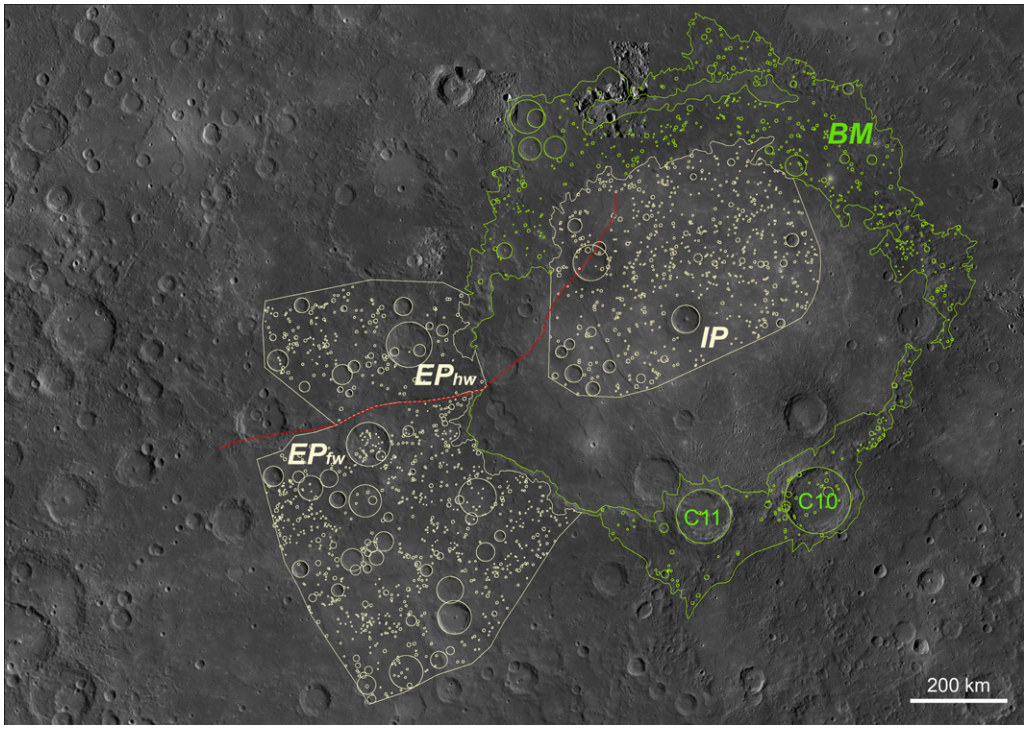

Fig. 3. Units in the Rembrandt basin region for which crater counts were performed, overlain on the MDIS 750 nm mosaic (average spatial resolution: 250 m/pixel). The red dashed line marks the leading edge of the Enterprise Rupes system. The green line bounds the crater-counting area of basin-related materials (i.e. the Hummocky Material and Proximal Ejecta units) labelled as *BM*, and green circles indicate craters counted within this area. White lines bound the crater-counting areas of units affected by resurfacing: the IPa sub-unit counting area within the Rembrandt basin is labelled as *IP*; counting areas located exterior to the basin are labelled EP_{fw} at the footwall of Enterprise Rupes and EP_{hw} at the hanging wall of the scarp; white circles indicate craters counted within this unit.

MESSENGER mosaic (average spatial resolution of 250 m/pixel). We outlined craters in our study areas using the ESRI ArcMap CraterTools extension developed by Kneissl *et al.* (2011), which accommodates distortion in crater shape due to non-shape-preserving map projections. Since the crater-age determination is based on primary craters (i.e. those formed by impacts with objects in heliocentric orbits; Melosh 1989), we avoided the inclusion of clusters and chains of craters that may be the result of secondary impacts. The effect of the contribution of far-field secondaries, which are normally not distinguishable from primary craters (e.g. McEwen & Bierhaus 2006), has not been considered.

In order to assess the Calorian age of the Rembrandt basin (*c.* 3.9 Ga) suggested by previous workers (Watters *et al.* 2009*a*; Fassett *et al.* 2012), we first performed a count of the primary craters of the Rembrandt basin-related units. Basin-proximal ejecta are presumed to have formed instantaneously within the Mercurian geological record (Spudis & Guest 1988), implying a production of fractured material comparable to the production within the basin rim. Thus, we merged the Hummocky Material and Proximal Ejecta into a single allostratigraphic unit, which served to increase the statistical robustness of our count. Craters counted in this unit are shown in Figure 3. The resultant crater SFD shows a distinct S-shaped kink for crater diameters between 17 and 30 km (Fig. 4a), which in this specific case cannot be correlated to any observable volcanic resurfacing.

The age of the basin's formation, as suggested by Watters *et al.* (2009*a*), has justified our use of the population of Main Belt Asteroids (MBA) as the prime source of impactors in our MPF analysis as it best accounts for the cratering distributions found for the oldest terrains of Mercury (>3.8 Ga: Strom *et al.* 2005; Marchi *et al.* 2009, 2013*b*). The MPF curve that fits the crater SFD best (Fig. 4a) indicates an age of 3.8 $\pm$ 0.1 Ga and, as a function of the crater diameter range enclosed within the S-shaped kink of the crater SFD (i.e. 17–30 km), suggests a thickness of the upper heavily fractured layer of approximately 3.5 km (see Marchi *et al.*

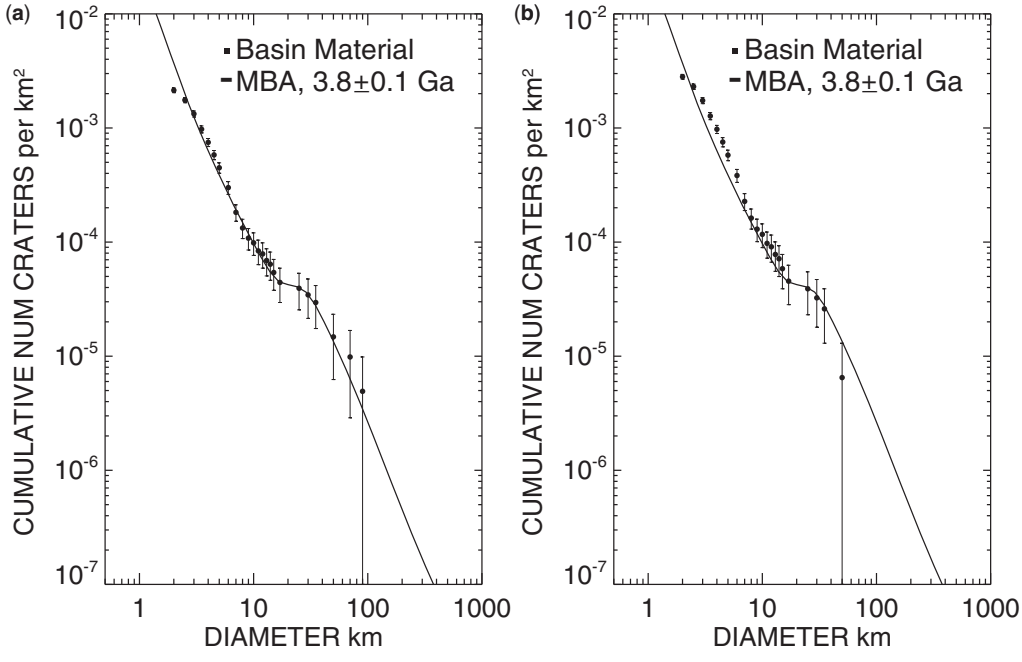

Fig. 4. MPF minimum χ^2 best fit of the cumulative crater-count distributions (applied binning scheme: 18 bins per diameter decade or steps 1.0, 1.1, 1.2, 1.3, 1.4, 1.5, 1.7, 2.0, 2.5, 3.0, 3.5, 4.0, 4.5, 5.0, 6.0, 7.0, 8.0, 9.0, 10.0 in the interval $1 \leq D \leq 10$) determined for the ejecta-related units (Hummocky Material and Proximal Ejecta) of the Rembrandt basin. For each unit we report the age assessment for Main Belt Asteroid populations. Error bars correspond to a variation of the minimum χ^2 of $\pm$50%. (**a**) The best-fit line obtained in the diameter range 5–100 km for the combined Hummocky Material and Proximal Ejecta units when considering fractured layers (i.e. cohesive material) of 3.5 km thickness over hard basement. (**b**) The best-fit line of these basin-related materials obtained after subtracting the two major craters (C10 and C11) in the diameter range 7–60 km, using the same target assumptions as for the best-fit line shown in (a).

2011). This is consistent with depth values of the transition between fractured near-surface rocks and the underlying intact material suggested by Schultz (1993) for conditions applicable to Mercury.

The occurrence of several very large craters in a relatively small area could give rise to a statistical effect that would appear as a deflection of the SFD curve, which, in the context of MPF analysis, may lead to misleading conclusions regarding the target rheology and layering (see Kirchoff *et al.* 2013 for a detailed discussion). In order to exclude this effect, we therefore removed the two major craters present in the counting area of the basin-related material (C10 and C11 in Fig. 3, which are 97 and 79 km in diameter, respectively) from the crater SFD shown in Figure 4a. As shown in Figure 4b, the deflection in the crater SFD still persists, and so we therefore regard it as reflecting a genuine change in stratigraphy, with the Hummocky Material and Proximal Ejecta units probably comprised of mechanically weaker surface units overlying more competent units. Although we observe no evidence in support of resurfacing as the cause of the kink in the SFD, we nevertheless also applied the Neukum Production Function method (NPF: Neukum *et al.* 2001) to the complete basin crater SFD, which returned a broadly similar cratering model age of 3.85 Ga for the age of Rembrandt basin (Fig. 5).

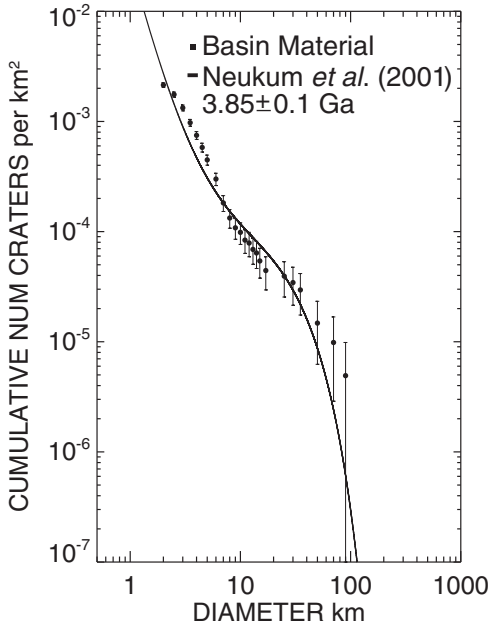

Fig. 5. The best-fit cratering model age of Rembrandt basin materials (i.e. Hummocky Material and Proximal Ejecta units) obtained in the diameter range 7–100 km using the production function and the chronology model of Neukum *et al.* (2001).

Next, we applied the MPF method to a portion of the central Interior Plains unit (Fig. 3). For the purposes of age calculation, we included the broadest portion of the Interior Plains but we did not consider the southern part of the unit, which hosts chains and clusters of secondary craters associated with the C10 and C11 impacts. The craters counted for this unit are shown in Figure 3. We identified, and included in our counting, several craters larger than 6–8 km in diameter that show evidence of partial burial, which we attribute to the resurfacing of the basin floor. Since this volcanic material is likely to be mechanically more cohesive than the upper fractured layer of the basin floor, we assumed the 'hard rock' scaling law (Holsapple & Housen 2007) for our MPF analysis.

The crater SFD of the portion of the Interior Plains unit we investigated shows a slight S-shaped kink for crater diameters between 8 and 12 km (Fig. 6a). The observational evidence for resurfacing (i.e. partially buried craters in Fig. 2) suggests that there may be two geologically distinct units – one atop the other – present within what we term the IPa sub-unit. Thus, we interpret this S-shaped kink as the product of a composite crater SFD that describes the resurfacing of an older unit by a younger, overlying unit. We therefore fit MPF curves both for craters larger than 12 km in diameter and for craters smaller than 8 km in diameter. The best MPF fit for larger craters corresponds to an age of 3.7 $\pm$ 0.1 Ga (Fig. 6a), whereas that for smaller craters corresponds to an age of 3.6 $\pm$ 0.1 Ga (Fig. 6b). Although the younger age of 3.6 $\pm$ 0.1 Ga is most probably overestimated – smaller crater bins are directly influenced by the larger craters of the distribution (Michael & Neukum 2010) – the obtained ages imply no statistical difference between the inferred layers.

This result does not clarify the nature of the inferred older layer, which, according to its MPF age (3.7 $\pm$ 0.1 Ga), could be either melt formed during the impact event or lava emplaced soon after basin formation. In any case, the crater population that formed on the older layer after basin formation defines the early production size–frequency to which the MPF is fit in Figure 6a. A subsequent resurfacing event was able to completely cover, and thus remove from the count, those craters whose depths were sufficiently shallow to be buried by this unit, but this phase of volcanism was of insufficient volume to completely bury craters above a given diameter (i.e. such that craters like those shown in Fig. 2 remain visible).

Hiesinger *et al.* (2002) suggested that the crater diameters in which S-shaped kinks exist in SFDs

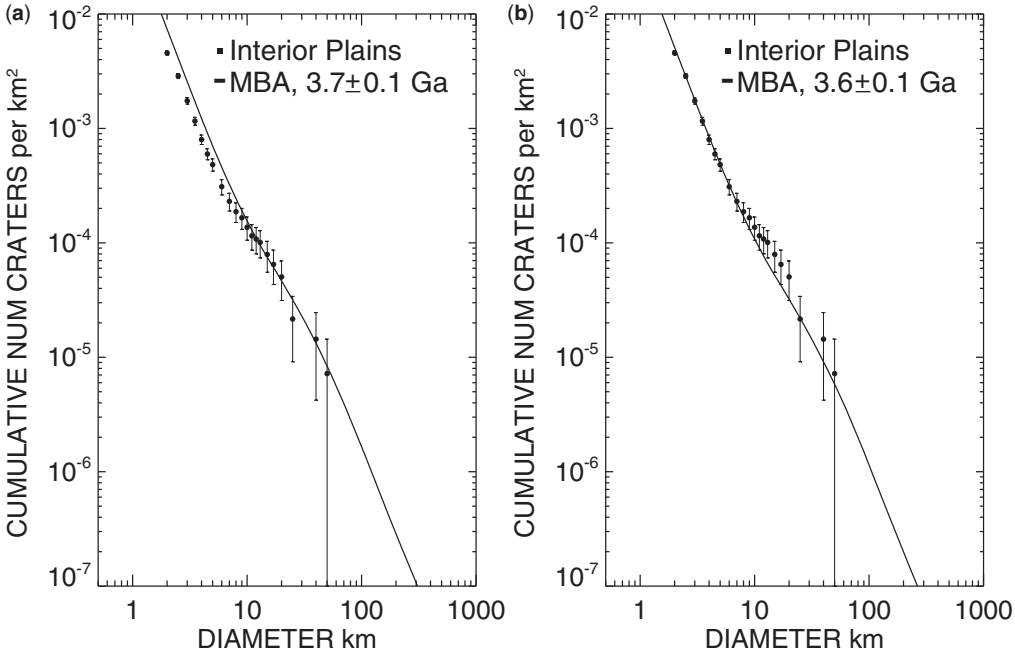

Fig. 6. MPF minimum χ^2 best fit determined for smooth plains interior to the basin. For each unit we report the age assessment for Main Belt Asteroid populations. Error bars correspond to a variation of the minimum χ^2 of ±50%. (**a**) MPF best-fit line for the IPa sub-unit counting area using larger craters (diameter fit range 10–60 km) obtained using hard rock as the target material. (**b**) MPF best-fit line for the same counting area, using smaller craters (diameter fit range 2–12 km) and, again, assuming a hard-rock target material.

where resurfacing has occurred are related to the thickness of the younger units. A deflection of an S-shaped kink that occurs at larger diameters corresponds to the extinction of smaller craters of the early crater population, whereas a deflection that occurs at smaller diameters corresponds to the post-flooding crater population (Hiesinger *et al.* 2002 and reference therein). Considering the rim height/diameter (h/D) relationship fixed for Mercury by Pike (1988), the crater diameters where these deflections occur can be used to estimate the minimum (h_{min}) and maximum (h_{max}) thicknesses of the younger IPa sub-unit. The h/D relationship (Pike 1988) depends on the interior morphology of the craters themselves, however, yielding two near-isometric trends on the basis of crater size:

$$h = 0.052\, D^{0.930} \quad \text{(for bowl-shaped craters with } 2.4\,\text{km} \leq D \leq 12\,\text{km}) \quad (4)$$

$$h = 0.150\, \mathrm{D}^{0.487} \quad \text{(for immature-complex craters with } 13\,\text{km} \leq D \leq 43\,\text{km}). \quad (5)$$

The standard errors of these relationships are ±0.08 km for equation (4) and ±0.13 km for equation (5) (Pike 1988). Using this approach, we obtained a minimum thickness, h_{min}, of 0.36 ± 0.08 km for the younger unit on the basis of the first crater SFD deflection at a crater diameter of 8 km (equation 4), and a maximum thickness, h_{max}, of 0.52 ± 0.13 km for the same unit when considering the second crater SFD deflection at crater diameters of 12 km (equation 5). However, the smallest partially buried craters we identified within the IPa sub-unit measure approximately 6 km in diameter. Therefore, given that craters less than 6 km in diameter should be considered to be totally buried, using equation (4) with $D = 6$ km, we derived a minimum thickness of the overlying infill of 0.28 ± 0.08 km, which is broadly consistent with previous results: Ernst *et al.* (2011) estimated a thickness of around 2 km for the high-reflectance plains that overlie the centre of the Rembrandt basin and that we mapped as IPa. This value was inferred on the basis of the maximum depth of post-resurfacing craters that do not appear to have exhumed low-reflectance material, which is assumed to underlie the high-reflectance plains (Ernst *et al.* 2010). We also performed crater counts on the terrains bordering the Rembrandt basin at its SW rim and at the footwall of Enterprise

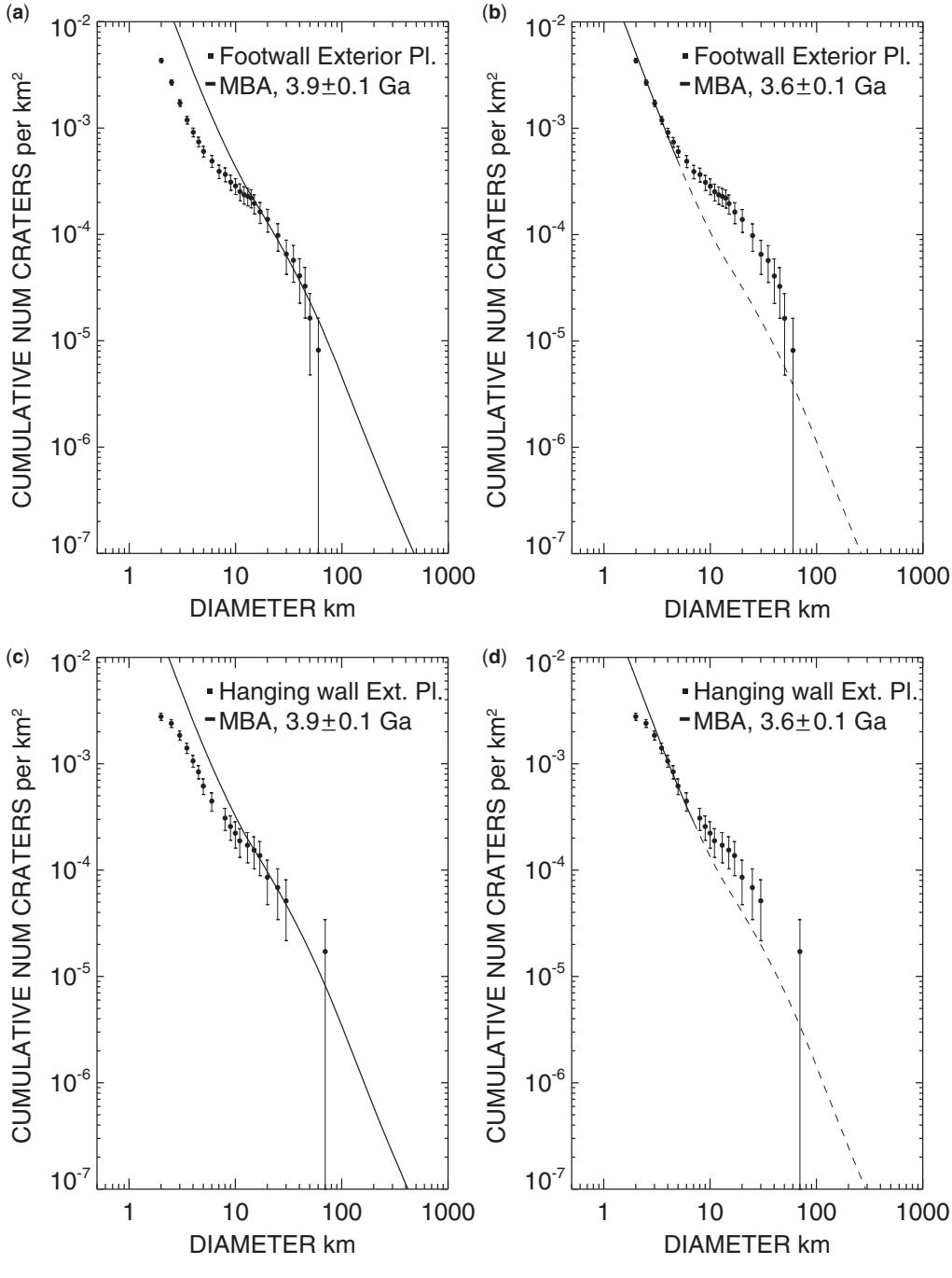

Fig. 7. MPF minimum χ^2 best fit determined for units exterior to the basin. As for previous figures, we report the age assessment for the Main Belt Asteroid populations. Error bars correspond to a variation of the minimum χ^2 of $\pm 50\%$. (**a**) The MPF best fit of larger craters of the EP_{fw} counting area (diameter fit range 12–70 km) obtained using hard rock as the target material. (**b**) The MPF best fit of smaller craters of the EP_{fw} counting area (diameter fit range 2–5 km) obtained using hard rock as the target material. (**c**) The MPF best fit of larger craters of the EP_{hw} counting area (diameter fit range 13–71 km) obtained using hard rock as the target material. (**d**) The MPF best fit of smaller craters of the EP_{hw} counting area (diameter fit range 3–6 km) obtained assuming hard rock as the target material.

Rupes ('Footwall' Exterior Plains, EP_{fw}: Fig. 3), which display textural and reflectance similarities to the Interior Plains unit. Craters counted in this area are shown in Figure 3, and probably include the largest secondary craters associated with the formation of the Rembrandt basin.

Since the EP_{fw} unit shows evidence of resurfacing (i.e. partially filled craters, shown with black arrows in Fig. 2), and given that the corresponding crater SFD shows an S-shaped kink for crater diameters between 4 and 14 km (Figs 7a & b), we applied the same analysis (i.e. under the assumption that a composite SFD is due to resurfacing) as for the IPa sub-unit. Owing to the broad kink, only a reduced portion of the SFD can be fitted by isochrones. We found that the best-fit MPF for larger craters returns an age of 3.9 ± 0.1 Ga (Fig. 7a), whereas, for smaller craters, the best-fit MPF yields an age of 3.6 ± 0.1 Ga (Fig. 7b).

As for the EP_{fw} unit, partially buried craters were identified atop the Enterprise Rupes contractional system (black arrows, Fig. 2). This terrain displays high-reflectance smooth surfaces associated with large craters (white arrows, Fig. 2), similar to the terrain at the base of Enterprise Rupes. We therefore applied the same approach as for EP_{fw} to the smooth area atop the Rupes ('Hanging wall' Exterior Plains, EP_{hw}: Fig. 3). This analysis returned an S-shaped crater SFD, kinked between 6 and 15 km, thus giving ages of 3.9 ± 0.1 Ga (Fig. 7c) for the older layer and 3.6 ± 0.1 Ga (Fig. 7d) for the younger layer.

The values for the EP_{hw} unit are identical (within error) to those found for the EP_{fw} unit. Using the crater h/D relationship (Pike 1988), we obtained a value for h_{min} for the overlying EP_{fw} unit of 0.19 ± 0.08 km, on the basis of the first crater SFD deflection at a crater diameter of 4 km (equation 4), and a h_{max} value for the EP_{fw} unit of 0.54 ± 0.13 km, on the basis of the second deflection at a crater diameter of 14 km (equation 5). A similar calculation for the overlying EP_{hw} unit yields a minimum thickness of 0.28 ± 0.08 km for the first crater SFD deflection at a crater diameter 6 km (equation 4), and a maximum thickness of 0.56 ± 0.13 km using the second deflection at a crater diameter of 15 km (equation 5). The results for the Exterior Plains units, especially the h_{max} estimates, are in close agreement with those calculated for the younger volcanic sub-unit of the Rembrandt basin's Interior Plains deposits (i.e. 0.36–0.52 km).

Discussion and conclusions

Using the Model Production Function method, we date the formation of the Rembrandt basin to 3.8 ± 0.1 Ga, in agreement with the age suggested by previous works (Watters *et al.* 2009*a*; Fassett *et al.* 2012). On the basis of MPF results, both of the ages of the units exterior to the Rembrandt basin we investigate (3.9 ± 0.1 and 3.6 ± 0.1 Ga) are within the uncertainty of the basin's age itself (3.8 ± 0.1 Ga). Terrains dated as 3.9 ± 0.1 Ga, therefore, may correspond to distal basin ejecta that partially covered pre-existing heavily cratered terrain (cf. Trask & Guest 1975). Since resurfacing has been recognized within the Rembrandt basin, all layers dated as 3.6 ± 0.1 Ga may be due to a later stage of volcanism. Within and surrounding the Caloris basin, MESSENGER data have revealed smooth plains that appear to be younger than the basin itself (Spudis & Guest 1988; Strom *et al.* 2008; Head *et al.* 2009; Fassett *et al.* 2012; Denevi *et al.* 2013), although definitive evidence that these plains are not of impact origin has yet to be found. The thermochemical convection models of Roberts & Barnouin (2012) suggest that the thermal impulse resulting from large impacts, such as that responsible for the Caloris basin, can alter the underlying mantle dynamics, producing subsequent volcanism far from the impact site. Such a scenario may also apply to the Rembrandt basin as the causative mechanism for the later phase of volcanism inferred for those units exterior to the basin rim.

However, on Mercury as on the Moon, it is likely that late-stage lavas also erupted from vents inside the basin, in particular along the margins of the basin floor, because of the likelihood of intense fracturing there that favours the ascent and eruption of magmas (Melosh 2011). In this case, it is possible that lavas that erupted within the basin may have spread beyond the rim, predating the development of parts of the system comprising Enterprise Rupes. Within the basin, the depletion of underlying magma reservoirs, coupled with the load of emplaced lavas, may have caused the basin floor to subside. Subsidence could have induced a first stage of horizontal shortening of the basin floor, forming contractional structures in the central Interior Plains unit (Watters *et al.* 2009*a*). In addition, the lava flows emplaced within the basin may have rapidly cooled, undergoing thermal contraction that could have produced antithetic normal faults within the basin, as has been found for smaller basins and craters (Freed *et al.* 2012; Blair *et al.* 2013).

While we provide observational evidence for volcanic resurfacing that affected the Rembrandt basin and its surroundings after basin formation, volcanism ended before the cessation of basin- and regional-scale tectonic deformation at 3.6 ± 0.1 Ga. Notably, deformation along other age-dated large scarp systems appears to have ceased at 3.7–3.6 Ga (e.g. Di Achille *et al.* 2012; Giacomini

et al. 2014), somewhat earlier than that along Enterprise Rupes.

The strain rate of global contraction of Mercury is still unclear. However, should the large Enterprise Rupes system have developed before the formation of the Rembrandt basin (e.g. Ferrari *et al.* 2012) during the LHB, regional-scale tectonism was active in this area from $>3.8 \pm 0.1$ Ga to beyond 3.6 ± 0.1 Ga. Recent analysis of Mercury's radius change using MESSENGER data indicates that Mercury experienced far more contraction than previously recognized (Byrne *et al.* 2014). Dating surface units associated with large tectonic structures, as we have done here, elsewhere on Mercury will provide a more detailed understanding of the global tectonic history of the innermost planet.

This research was supported by the Italian Space Agency (ASI) within the SIMBIOSYS Project (ASI-INAF agreement No. I/022/10/0) and by P. di Ateneo CPDA 112213/11 of the University of Padua. P.K. Byrne and C. Klimczak acknowledge support from the MESSENGER project, which in turn is supported by the NASA Discovery Program under contracts NASW-00002 to the Carnegie Institution of Washington and NAS5–97271 to the Johns Hopkins University Applied Physics Laboratory. We thank Mario D'Amore for improving the layout of plots. Careful reviews by B.W. Denevi, T. Platz and an anonymous reviewer substantially improved this manuscript.

References

Blair, D. M., Freed, A. M. *et al.* 2013. The origin of graben and ridges in Rachmaninoff, Raditladi, and Mozart basins, Mercury. *Journal of Geophysical Research: Planets*, **118/1**, 47–58, http://dx.doi.org/10.1029/2012JE004198

Blewett, D. T., Hawke, B. R., Lucey, P. G. & Robinson, M. S. 2007. A Mariner 10 color study of mercurian craters. *Journal of Geophysical Research: Planets*, **112**(E2), E02005, http://dx.doi.org/10.1029/2006JE002713

Byrne, P. K., Watters, T. R., Murchie, S. L., Klimczak, C., Solomon, S. C., Prockter, L. M. & Freed, A. M. 2012. A tectonic survey of the Caloris basin, Mercury. *In*: *43rd Lunar and Planetary Science Conference, held March 19–23, 2012 at The Woodlands, Texas*. Lunar and Planetary Institute, Houston, TX, Abstract 1722.

Byrne, P. K., Klimczak, C. *et al.* 2013. Tectonic complexity within volcanically infilled craters and basins on Mercury. *In*: *44th Lunar and Planetary Science Conference, held March 18–22, 2013 at The Woodlands, Texas*. Lunar and Planetary Institute, Houston, TX, Abstract 1261.

Byrne, P. K., Klimczak, C., Şengor, A. M. C., Solomon, S. C., Watters, T. R. & Hauck, S. A., II 2014. Mercury's global contraction much greater than earlier estimates. *Nature Geoscience*, **7**, 301–307.

Cintala, M. & Grieve, R. 1998. Scaling impact melting and crater dimensions: Implications for the lunar cratering record. *Meteoritics and Planetary Science*, **33**, 889–912.

Denevi, B. W., Robinson, M. S. *et al.* 2009. The evolution of Mercury's crust: a global perspective from MESSENGER. *Science*, **324**, 613–618.

Denevi, B. W., Ernst, C. M. *et al.* 2013. The distribution and origin of smooth plains on Mercury. *Journal of Geophysical Research: Planets*, **118**, 891–907, http://dx.doi.org/10.1002/jgre.20075

Di Achille, G., Popa, C., Massironi, M., Mazzotta Epifani, E., Zusi, M., Cremonese, G. & Palumbo, P. 2012. Mercury's radius change estimates revisited using MESSENGER data. *Icarus*, **221**, 456–460.

Dzurisin, D. 1978. Tectonic and volcanic chronology of Mercury as inferred from studies of scarps, ridges, troughs, and other lineaments. *Journal of Geophysical Research*, **83**, 4883–4906.

Ernst, C. M., Murchie, S. L. *et al.* 2010. Exposure of spectrally distinct material by impact craters on Mercury: Implications for global stratigraphy. *In*: Blewett, D. T., Hauck, S. A. & Korth, H. (eds) *Mercury after Two MESSENGER Flybys*. *Icarus*, **209**, 210–223.

Ernst, C. M., Murchie, S. L. *et al.* 2011. Thickness of volcanic fill in impact basin on Mercury. *In*: *Geological Society of America 2011 Annual Meeting: Archean to Anthropocene: The Past is the Key to the Future, 9–12 October 2011, Minneapolis, Minnesota*. Geological Society of America, Boulder, CO, Abstract 142-8.

Fasset, C. I., Head, J. W. *et al.* 2009. Caloris impact basin: exterior geomorphology, stratigraphy, morphometry, radial sculpture, and smooth plains deposits. *Earth and Planetary Science Letters*, **285**, 297–308.

Fassett, C. I., Head, J. W. *et al.* 2012. Large impact basins on Mercury: global distribution, characteristics, and modification history from MESSENGER orbital data. *Journal of Geophysical Research: Planets*, **117/E12**, E00L08, http://dx.doi.org/10.1029/2012JE004154

Ferrari, S., Massironi, M., Klimczak, C., Byrne, P. K., Cremonese, G. & Solomon, S. C. 2012. Complex history of the Rembrandt basin and scarp system, Mercury. *In*: *European Planetary Science Congress 2012, held 23–28 September, 2012, Madrid, Spain*. Copernicus, Göttingen, Abstract EPSC-2012-874.

Freed, A. M., Blair, D. M. *et al.* 2012. On the origin of graben and ridges within and near volcanically buried craters and basins in Mercury's northern plains. *Journal of Geophysical Research: Planets*, **117/E12**, E00L06, http://dx.doi.org/10.1029/2012JE004119

Giacomini, L., Massironi, M., Marchi, S., Fassett, C. I., Di Achille, G. & Cremonese, G. 2014. Age dating of an extensive thrust system on Mercury: implications for the planet's thermal evolution. *In*: Platz, T., Massironi, M., Byrne, P. K. & Hiesinger, H. (eds) *Volcanism and Tectonism Across the Inner Solar System*. Geological Society, London, Special Publications, **401**. First published online August 13, 2014, http://dx.doi.org/10.1144/SP401.21

Hawkins, S. E., Boldt, J. D. *et al.* 2007. The Mercury Dual Imaging System on the MESSENGER Spacecraft. *Space Science Review*, **131**, 247–338, http://dx.doi.org/10.1007/s11214-007-9266-3

Head, J. W., Murchie, S. L. *et al.* 2009. Volcanism on Mercury: evidence from the first MESSENGER flyby for extrusive and explosive activity and the volcanic origin of plains. *Earth and Planetary Science Letters*, **285**, 227–242.

Head, J. W., Chapman, C. R. *et al.* 2011. Flood volcanism in the northern high latitudes of Mercury revealed by MESSENGER. *Science*, **333**, 1853–1856.

Hiesinger, H., Head, J. W., Wolf, U., Jaumann, R. & Neukum, G. 2002. Lunar mare basalt flow units: thicknesses determined from crater size-frequency distributions. *Geophysical Research Letters*, **29**, 8, http://dx.doi.org/10.1029/2002GL014847

Holsapple, K. A. & Housen, K. R. 2007. A crater and its ejecta: an interpretation of Deep Impact. *In*: Combi, M. R. & A'Hearn, M. F. (eds) *Deep Impact Mission to Comet 9P/Tempel 1, Part 1. Icarus*, **187**(1), 345–356.

Hörz, F., Grieve, R., Heiken, G., Spudis, P. & Binder, A. 1991. Lunar surface processes. *In*: Heiken, G. H., Vaniman, D. T. & French, B. M. (eds) *Lunar Source Book: A User's Guide to the Moon*. Cambridge University Press, Cambridge, 61–120.

Kirchoff, M. R., Chapman, C. R., Marchi, S., Curtis, K. M., Enke, B. & Bottke, W. F. 2013. Ages of large lunar impact craters and implications for bombardment during the Moon's middle age. *Icarus*, **225**, 325–341.

Klimczak, C., Schultz, R. A. & Nahm, A. L. 2010. Evaluation of the origin hypotheses of Pantheon Fossae, central Caloris basin, Mercury. *Icarus*, **209**, 262–270, http://dx.doi.org/10.1016/j.icarus.2010.04.014

Klimczak, C., Watters, T. R. *et al.* 2012. Deformation associated with ghost craters and basins in volcanic smooth plains on Mercury: strain analysis and implications for plains evolution. *Journal of Geophysical Research: Planets*, **117** (E12), E00L03, http://dx.doi.org/10.1029/2012JE004100

Kneissl, T., van Gasselt, S. & Neukum, G. 2011. Map-projection-independent crater size-frequency determination in GIS environments – new software tool for Arc-GIS. *Planetary and Space Science*, **59**, 1243–1254.

Marchi, S., Mottola, S., Cremonese, G., Massironi, M. & Martellato, E. 2009. A new chronology for the Moon and Mercury. *Astronomical Journal*, **137**, 4936–4948.

Marchi, S., Massironi, M., Cremonese, G., Martellato, E., Giacomini, L. & Prockter, L. 2011. The effects of the target material properties and layering on the crater chronology: the case of Raditladi and Rachmaninoff basins on Mercury. *Planetary and Space Science*, **59**, 1968–1980.

Marchi, S., Bottke, W. F., Kring, D. A. & Morbidelli, A. 2012. The onset of the lunar cataclysm as recorded in its ancient crater populations. *Earth and Planetary Science Letters*, **325**, 27–38.

Marchi, S., Bottke, W. F. *et al.* 2013*a*. High-velocity collisions from the lunar cataclysm recorded in asteroidal meteorites. *Nature Geoscience*, **6**, 303–307.

Marchi, S., Chapman, R. C., Fassett, C. I., Head, J. W., Bottke, W. F. & Strom, R. G. 2013*b*. Global resurfacing of Mercury 4.0–4.1 billion years ago by heavy bombardment and volcanism. *Nature*, **499**, 59–61.

Massironi, M., Cremonese, G., Marchi, S., Martellato, E., Mottola, S. & Wagner, R. J. 2009. Mercury's geochronology revised by applying Model Production Function to Mariner 10 data: geological implications. *Geophysical Research Letters*, **36**, L21204, http://dx.doi.org/10.1029/2009GL040353

Massironi, M., Di Achille, G. *et al.* 2014. Lateral ramps and strike-slip kinematics on Mercury. *In*: Platz, T., Massironi, M., Byrne, P. K. & Hiesinger, H. (eds) *Volcanism and Tectonism Across the Inner Solar System*. Geological Society, London, Special Publications, **401**. First published online June 5, 2014, http://dx.doi.org/10.1144/SP401.16

McEwen, A. S. & Bierhaus, E. B. 2006. The importance of secondary cratering to age constraints on planetary surfaces. *Annual Reviews of Earth and Planetary Sciences*, **34**, 535–567.

Melosh, H. J. 1989. *Impact Cratering: A Geological Process*. Oxford Monographs on Geology and Geophysics, **11**. Oxford University Press, New York.

Melosh, H. J. 2011. Impact cratering. *In*: Melosh, H. J. (ed.) *Planetary Surface Processes*. Purdue University, West Lafayette, IN, 222–275.

Melosh, H. J. & Dzurisin, D. 1978. Mercurian global tectonics: a consequence of tidal despinning? *Icarus*, **35**, 227–236.

Melosh, H. J. & McKinnon, W. B. 1988. The tectonics of Mercury. *In*: Vilas, F., Chapman, C. R. & Matthews, M. S. (eds) *Mercury*. University of Arizona Press, Tucson, AZ, 374–400.

Michael, G. G. & Neukum, G. 2010. Planetary surface dating from crater size-frequency distribution measurements: partial resurfacing events and statistical age uncertainty. *Earth and Planetary Science Letters*, **294**, 223–229.

Murchie, S. L., Watters, T. R. *et al.* 2008. Geology of the Caloris basin, Mercury: a new view from MESSENGER. *Science*, **321**, 73–76.

Neukum, G. & Horn, P. 1975. Effects of lava flows on lunar crater populations. *The Moon*, **15**, 205–222.

Neukum, G., Oberst, J., Hoffmann, H., Wagner, R. & Ivanov, B. A. 2001. Geologic evolution and cratering history of Mercury. *Planetary and Space Science*, **49**, 1507–1521.

Pike, R. J. 1988. Geomorphology of impact craters on Mercury. *In*: Vilas, F., Chapman, C. R. & Matthews, M. S. (eds) *Mercury*. University of Arizona Press, Tucson, AZ, 165–273.

Platz, T., Michael, G., Tanaka, K. L., Skinner, J. A. & Fortezzo, C. M. 2013. Crater-based dating of geological units on Mars: methods and application for the new global geological map. *Icarus*, **225**, 806–825.

Prockter, M. L., Ernst, C. M. *et al.* 2010. Evidence for young volcanism on Mercury from the third MESSENGER flyby. *Science*, **329**, 668–671.

Roberts, J. H. & Barnouin, O. S. 2012. The effect of the Caloris impact on the mantle dynamics and volcanism of Mercury. *Journal of Geophysical Research: Planets*, **117/E2**, E02007, http://dx.doi.org/10.1029/2011JE003876

ROBINSON, M. S. & LUCEY, P. G. 1997. Recalibrated Mariner 10 color mosaics: implications for Mercurian volcanism. *Science*, **275**, 197–200.

ROBINSON, M. S., MURCHIE, S. L. *ET AL.* 2008. Reflectance and color variations on Mercury: indicators of regolith processes and compositional heterogeneity. *Science*, **321**, 66–69.

SCHULTZ, R. A. 1993. Brittle strength of basaltic rock masses with applications to Venus. *Journal of Geophysical Research: Planets*, **98/E6**, 10 883–10 895, http://dx.doi.org/10.1029/93JE00691

SPUDIS, P. D. & GUEST, J. E. 1988. Stratigraphy and geologic history of Mercury. *In*: VILAS, F., CHAPMAN, C. R. & MATTHEWS, M. S. (eds) *Mercury*. University of Arizona Press, Tucson, AZ, 118–164.

STROM, R. G. & NEUKUM, G. 1988. The cratering record on Mercury and the origin of impacting objects. *In*: VILAS, F., CHAPMAN, C. R. & MATTHEWS, M. S. (eds) *Mercury*. University of Arizona Press, Tucson, AZ, 336–373.

STROM, R. G., TRASK, N. J. & GUEST, J. E. 1975. Tectonism and volcanism on Mercury. *Journal of Geophysical Research*, **80**, 2478–2507.

STROM, R. G., MALHOTRA, R., ITO, T., YOSHIDA, F. & KRING, D. A. 2005. The origin of planetary impactors in the inner solar system. *Science*, **309**, (5742), 1847–1850.

STROM, R. G., CHAPMAN, C. R., MERLINE, W. J., SOLOMON, S. C. & HEAD, J. W. 2008. Mercury cratering record viewed from MESSENGER's first flyby. *Science*, **321**, 79–81.

TERA, F., PAPANASTASSIOU, D. A. & WASSERBURG, G. J. 1974. Isotopic evidence for a terminal lunar cataclysm. *Earth and Planetary Science Letters*, **22**, 1–21.

TOKSÖZ, M. N., PRESS, F. *ET AL.* 1972. Structure composition and properties of lunar crust. *In*: *Proceedings of the Third Lunar Science Conference, Houston, Texas, January 10–13, 1972, Sponsored by the Lunar Science Institute, Volume 3*. MIT Press, Cambridge, MA, 2527–2544.

TRASK, N. J. & GUEST, J. E. 1975. Preliminary geologic terrain map of Mercury. *Journal of Geophysical Research*, **80**, 2461–2477.

WATTERS, T. R. & NIMMO, F. 2010. The tectonics of Mercury. *In*: WATTERS, T. R. & SCHULTZ, R. A. (eds) *Planetary Tectonics*. Cambridge University Press, Cambridge, 15–79.

WATTERS, T. R., ROBINSON, M. S., BINA, C. R. & SPUDIS, P. D. 2004. Thrust faults and the global contraction of Mercury. *Geophysical Research Letters*, **31**, L04071.

WATTERS, T. R., NIMMO, F. & ROBINSON, M. S. 2005. Extensional troughs in the Caloris Basin of Mercury: evidence of lateral crustal flow. *Geology*, **33**, 669–672.

WATTERS, T. R., HEAD, J. W. *ET AL.* 2009*a*. Evolution of the Rembrandt Impact Basin on Mercury. *Science*, **324**, 618–621.

WATTERS, T. R., MURCHIE, S. L., ROBINSON, M. S., SOLOMON, S. C., DENEVI, B. W., ANDRÉ, S. L. & HEAD, J. W. 2009*b*. Emplacement and tectonic deformation of smooth plains in the Caloris basin, Mercury. *Earth and Planetary Science Letters*, **285**, 309–319.

WATTERS, T. R., SOLOMON, S. C., ROBINSON, M. S., HEAD, J. W., ANDRÈ, S. L., HAUCK, S. A. & MURCHIE, S. L. 2009*c*. The tectonics of Mercury: the view after MESSENGER's first flyby. *Earth and Planetary Science Letters*, **285**, 283–296.

WATTERS, T. R., SOLOMON, S. C. *ET AL.* 2012. Extension and contraction within volcanically buried impact craters and basins on Mercury. *Geology*, **40**, 1123–1126, http://dx.doi.org/10.1130/G33725.1